LANGMUIR

pubs.acs.org/Langmuir Article

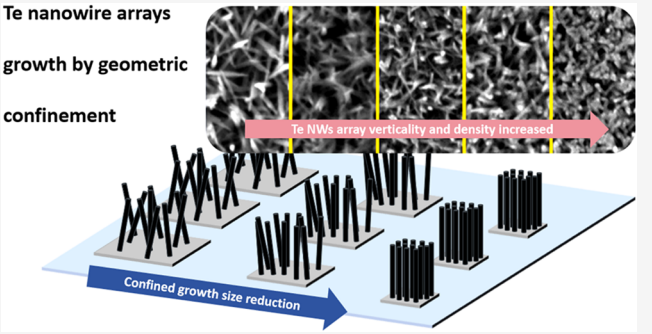
Vertically Aligned Te Nanowire Array Growth by Geometric Confinement

Xiaobing Zhu,[⊥] Moneeb Zafar,[⊥] Yanmei Ren, Rongke Sun, Rui Li, Xin He, Yanqing Ma,* and Lei Ma*

Cite This: *Langmuir* 2026, 42, 29121−29130 Read Online

ACCESS | Metrics & More | Article Recommendations | Supporting Information

ABSTRACT: Tellurium nanowires have demonstrated great potential for various applications, such as thermoelectric devices, optoelectronics, and biosensors, due to their excellent electronic, thermal, and optical properties. However, lacking an effective method to prepare vertically aligned and uniformly distributed tellurium nanowire arrays is a bottleneck for their practical applications. In this study, we successfully fabricated aligned tellurium nanowires (A-Te NWs) on a Pt/polyimide/glass substrate using a seedless chemical liquid-phase method. Pt square arrays were employed as the catalytic layer to define patterned selective growth regions on the polyimide/glass substrate. Such geometric confinement of growth proves highly effective in promoting the vertical ordering of A-Te NWs. Moreover, the verticality and density of A-Te NWs highly depend on the Pt pattern size. Specifically, smaller patterns result in denser and more vertical A-Te NWs due to their lower surface roughness. In addition, the Pt layer thickness and liquid-phase reaction conditions for the growth of A-Te NWs have been optimized to yield densely packed and vertically aligned A-Te NWs, with a Pt layer thickness of 3 nm, a reaction time of 6 h, a reaction temperature of 30 °C, a pH of 10, a hydrazine hydrate amount of 2 mL, and a cetyltrimethylammonium bromide concentration of 5 mM. Our work paves the way for the practical applications of tellurium nanowires.



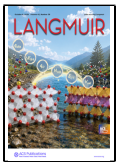
INTRODUCTION

Tellurium nanowires (Te NWs) have gained widespread attention in the scientific community due to their unique electronic, thermal, and optical properties.[1] They also demonstrate great potential for various applications, such as thermoelectric devices, optoelectronics, and biosensors.[1,2]

Vertically aligned NW arrays enable efficient utilization of the ultrahigh carrier mobility of Te along the crystallographic *c*-axis. Both theoretical calculations and experimental measurements have demonstrated that the hole mobility in single-crystalline Te NWs along the helical chain direction (the *c*-axis) can reach several hundred $cm^2 \cdot V^{-1} \cdot s^{-1}$, exceeding the performance limits of conventional amorphous silicon and even polycrystalline silicon thin-film transistors.[3] In a vertically oriented configuration, the carrier transport path is well aligned with the electric field direction, effectively avoiding the severe mobility degradation caused by grain-boundary scattering, non-uniform contact barriers, and tortuous conduction pathways commonly encountered in randomly oriented or laterally lying NW networks. Furthermore, uniform distribution is a prerequisite for achieving statistical consistency of device parameters and for enabling large-scale integration. In thin-film devices, significant variations in NW length, diameter, or spacing can directly lead to wide distributions of key parameters such as channel resistance, threshold voltage, and subthreshold swing. For instance, differences in NW length alter the effective channel length and thus affect the on-state current, while diameter variations change the relative contribution of surface depletion, giving rise to threshold voltage shifts.[4] Therefore, the ability to obtain vertically aligned and uniformly distributed Te NW arrays is essential for realizing high-performance, reproducible, and integrable devices. However, one of the critical challenges that hinders the widespread adoption of Te NWs in practical applications is the lack of effective methods to achieve vertically aligned and uniformly distributed nanowire arrays.[5]

Over the years, a number of growth techniques have been employed to synthesize Te NWs, including vapor-liquid-solid (VLS) processes, hydrothermal methods, and electrodeposition methods.[6−8] Although these methods offer reasonable control over the basic parameters (such as diameter and length) of Te NWs, they often fail to provide satisfactory results concerning the alignment and vertical orientation of NWs.[9] Given that achieving well-aligned Te NW arrays is

Received: June 23, 2026
Revised: September 9, 2026
Accepted: September 9, 2026
Published: September 21, 2026



ACS Publications © 2026 American Chemical Society

https://doi.org/10.1021/acs.langmuir.6c03602
Langmuir 2026, 42, 29121−29130

Downloaded from pubs.acs.org/langd5/article-pdf/42/39/29121/6858872/1/acs.langmuir.6c03602.pdf by TIANJIN UNIV user on 11 November 2026

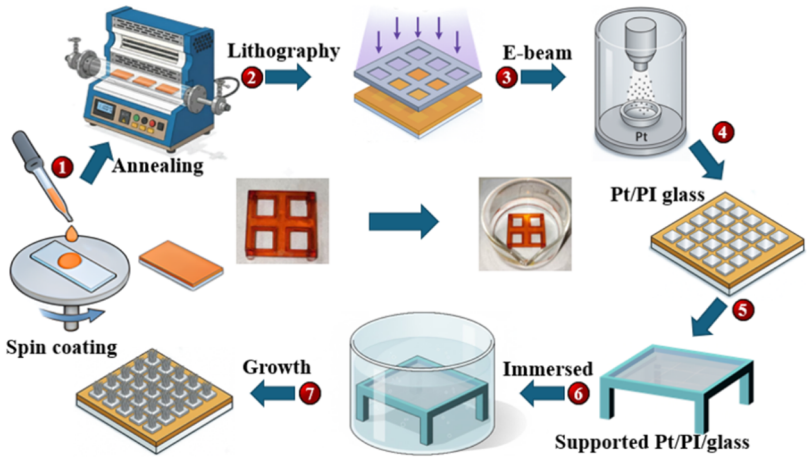


Figure 1. Schematic and physical photographs of the synthesis of A-Te NWs on Pt/PI/glass substrates.

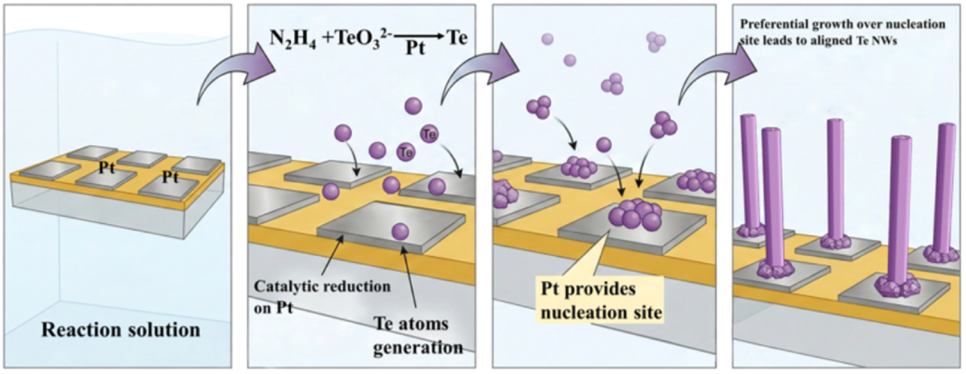


Figure 2. Schematic of the seedless low-temperature wet growth process of A-Te NWs on patterned Pt/PI/glass substrates.

particularly crucial for leveraging the anisotropic properties of Te NWs in device applications, controlled and aligned growth of Te NWs becomes imperative.[10,11]

In this regard, confined growth techniques have garnered significant interest for their ability to direct nanostructure growth in specific orientations.[12] Normally, confined growth involves using a template or a patterned substrate to guide the material's growth, thereby improving the orientation and arrangement of the nanostructures.[13] The existing literature has reported the use of various substrates, such as anodized aluminum oxide (AAO) membranes, for this purpose.[14] However, confined growth techniques have rarely been applied to the growth of highly aligned Te NWs.[15]

In addition, chemical liquid-phase methods could be promising for solving the alignment issue in growing A-Te NWs, since they are scalable and offer a higher degree of control over multiple parameters. Most importantly, they can accommodate patterned catalyst layers, which can effectively guide the directional growth of Te NWs.[16] Among potential catalysts, platinum (Pt) is highly stable and offers excellent catalytic properties in liquid-phase reactions.[17] Moreover, the advantages of using a patterned Pt layer in confined growth scenarios extend beyond the prospects of alignment and orientation.[18,19] Therefore, employing patterned Pt layers in the confined liquid-phase growth may yield highly aligned Te NWs.[20] However, this approach remains largely unexplored.[21]

In this study, using a geometrically confined liquid-phase method and patterned catalyst Pt layers, densely packed and vertically aligned Te NW arrays have been successfully grown on Pt/polyimide (PI)/glass substrates.[22] The verticality and density of A-Te NWs were found to strongly depend on the Pt pattern size, with smaller Pt patterns corresponding to denser and more vertical Te NWs owing to their lower surface roughness. Furthermore, the effects of the Pt layer thickness and liquid-phase reaction conditions on the growth of Te NW arrays have been systematically investigated. The optimal growth parameters were determined as follows: Pt layer thickness of 3 nm, a reaction time of 6 h, a reaction temperature of 30 °C, a pH of 10, a hydrazine hydrate amount of 2 mL, and a cetyltrimethylammonium bromide (CTAB) concentration of 5 mM. This innovative approach could enhance packing density, mechanical stability, and directional properties of Te NW arrays, thus enabling their device integration and functional applications.[23]

RESULTS AND DISCUSSION

Synthesis, Characterization, and Growth Mechanism of A-Te NWs on Pt/Polyimide/Glass Substrate

Aligned Te NWs (A-Te NWs) were grown on Pt/PI/glass using a method very similar to that used for template-free growth on Pt/FTO/glass.[10] Pt squares with different sizes were patterned on the PI/glass substrate by photolithography and electron beam evaporation (Figure 1). A more detailed description of the synthesis can be found in the Experimental Procedures Section.

The seedless chemical liquid-phase growth process with patterned Pt as the substrate is shown in Figure 2. The

https://doi.org/10.1021/acs.langmuir.6c03602
Langmuir 2026, 42, 29121−29130

Downloaded from pubs.acs.org/langd5/article-pdf/42/39/29121/6858872/1/acs.langmuir.6c03602.pdf by TIANJIN UNIV user on 11 November 2026

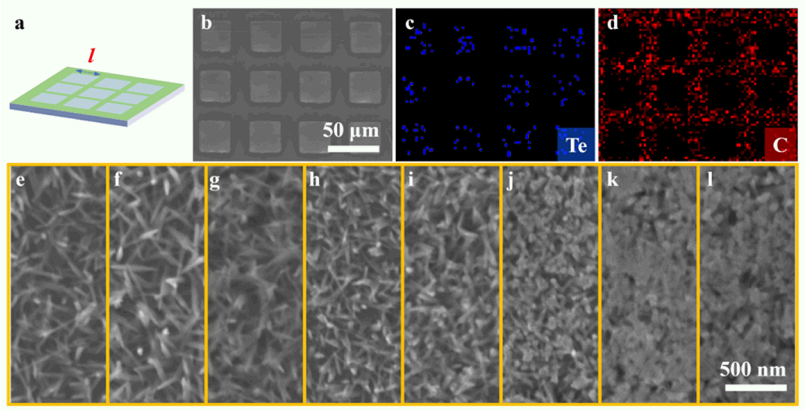


Figure 3. (a) Schematic of the patterned Pt/PI/glass substrate. (b) SEM images of the A-Te NWs/Pt/PI/glass. EDS elemental distributions of (c) Te elements and (d) C elements. SEM images of A-Te NWs grown on square Pt patterns with side lengths of (e) 1024 μm, (f) 512 μm, (g) 256 μm, (h) 128 μm, (i) 64 μm, (j) 32 μm, (k)16 μm, and (l) 8 μm (the scale bar is 500 nm).

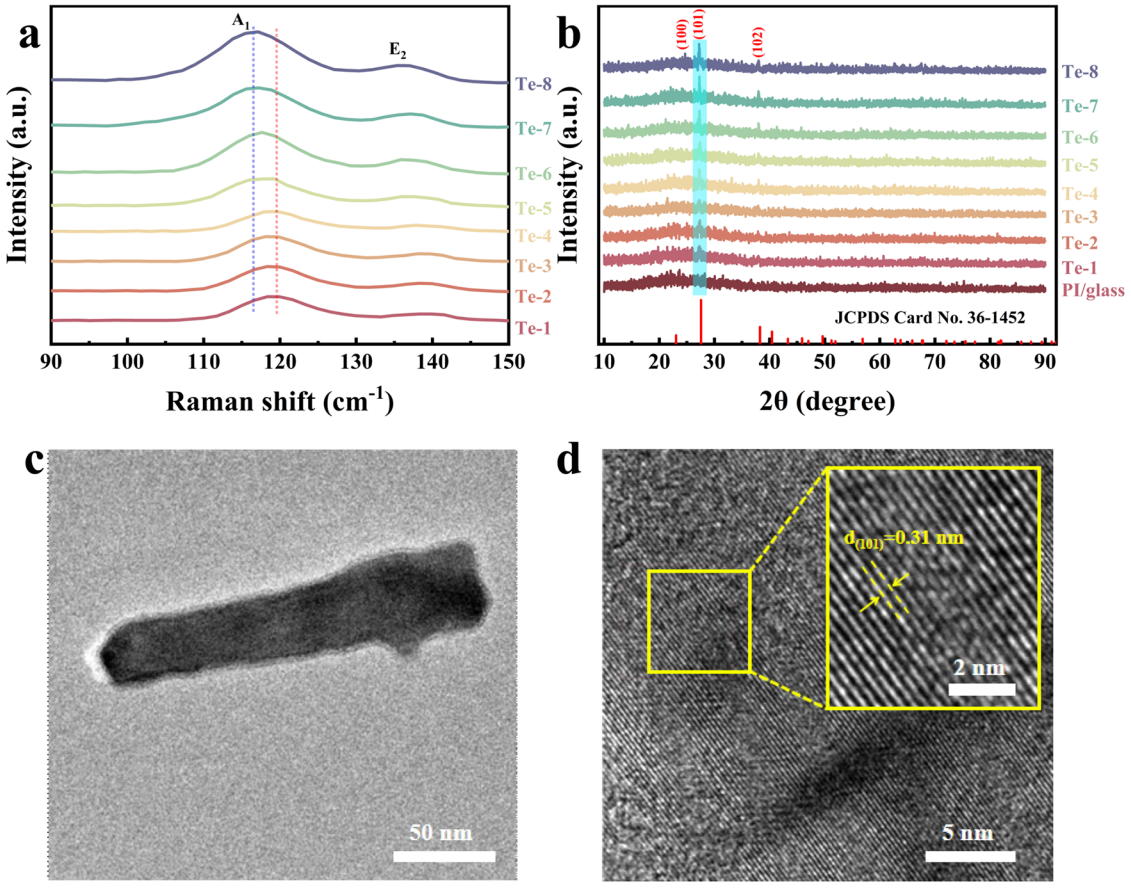


Figure 4. (a) Raman spectra and (b) XRD patterns of samples grown on Pt patterns with different edge lengths; (c) TEM images of Te NWs and (d) HRTEM images of local regions.

synthesis process begins with the immersion of a patterned Pt/PI glass substrate in a reaction solution. After the Te precursor in the solution generates active Te atoms under the action of the reducing agent, it is preferentially adsorbed and enriched on the Pt surface.[24] The adsorption of Te on Pt surfaces typically involves strong chemical interactions.[25] Our theoretical calculations reveal that the adsorption energy of a Te atom on the Pt surface is 4.91 eV, while the migration energy barrier of Te on the Pt surface is only 0.22 eV (Figure S1a). Meanwhile, we also calculated the adsorption energy (3.36 eV) and migration energy barrier (0.15 eV) of Te on the Au surface, and the corresponding migration-process models are presented in Figure S1b−f. Computational analysis indicates that the Te−Au bond is much weaker than the Te−Pt bond. Figure S1g shows that the Pt surface is fully covered by Te NWs and appears black, whereas the Au surface retains metallic luster without nanowire coverage. It is verified that the Au surface (Figure S1h,i) has no Te NW growth but only agglomerated Te spheres that originate from the precursor.[20] As Pt has a strong affinity for Te and a high surface energy, it

https://doi.org/10.1021/acs.langmuir.6c03602
Langmuir 2026, 42, 29121−29130

Downloaded from pubs.acs.org/langd5/article-pdf/42/39/29121/6858872/1/acs.langmuir.6c03602.pdf by TIANJIN UNIV user on 11 November 2026

can significantly reduce the nucleation barrier of Te, leading to the formation of a Te enrichment layer or Pt−Te transition layer at the Pt/solution interface.[26] Subsequently, due to the chain structure and significant anisotropic growth characteristics of Te crystals, coupled with the selective inhibition of Pt and surfactant on lateral growth, the initial nuclei tend to grow preferentially along specific crystal directions and finally form Te nanowires with high aspect ratio.[20]

As shown in Figure 3a, a selective growth region was defined on the PI/glass substrate by depositing Pt on squares patterned on the substrate, where "*l*" is the edge length of the Pt square. Due to the decisive role of Pt in the growth of A-Te NWs as described above, A-Te NWs will only grow inside the Pt squares. A low-magnification SEM image of the A-Te NWs/Pt/PI/glass structure arrays is shown in Figure 3b. The distribution of A-Te NWs on the substrate was studied by analyzing the elemental distribution of Te through energy-dispersive spectrometer (EDS) mapping. Figure 3c and 3d illustrates the elemental distribution of Te and C on the substrate, respectively. The distribution of Te is confined within the square Pt patterns, whereas C, whose source is mainly the PI substrate, is mainly distributed in the gaps outside the square array. The above results indicate that the growth of A-Te NWs occurs within the Pt squares and no growth of Te takes place outside the Pt squares.

The geometrically confined domain in this experiment was achieved by lithographic patterning of Pt squares and adjusted by stepwise reducing their edge lengths. According to the different sizes of the initial single square Pt side lengths, the A-Te NWs/Pt/PI/glass samples were named Te-1, Te-2, Te-3, Te-4, Te-5, Te-6, Te-7, and Te-8 when the edge length was 1024, 512, 256, 128, 64, 32, 16, and 8 μm, respectively (Figure S2).

SEM images of A-Te NWs grown on square Pt arrays with different edge lengths are presented in Figure 3e−3l, revealing distinct morphological differences. NWs tend to grow vertically,[27,28] which is energetically favorable as it minimizes the overall surface energy of the system.[29] When the square edge length is 1024 μm, NWs are highly tilted (Figure 3e), and there are many empty regions. Since the confinement of the growth region into a small area forces the NWs to grow upright rather than at an incline, when the Pt edge length is decreased from 1024 to 256 μm, NWs exhibit similar surface morphologies (Figure 3f and 3g). When the length is decreased to 128 μm, both the density and the verticality of A-Te NWs are increased, with few void regions (Figure 3h). With further decrease in pattern size, the A-Te NWs exhibit enhanced vertical alignment with a more compact arrangement. For the patterns with an edge length of 64 and 32 μm, the NWs are highly vertical, as evident from the top-view SEM (Figure 3i and 3j), where only the tips of the NWs are discernible. However, when the geometrically confined growth region reaches the critical threshold of 16 and 8 μm (Figure 3k and 3l), the A-Te NWs merge at the top due to the extremely sharp increase in density.

Raman spectra and XRD patterns were employed to characterize the crystal structure of A-Te NW arrays. Figure 4a shows two active Raman phonon modes (A_1 and E_2) of Te,[20,30] and the A_1 peak is red-shifted with decreasing length of square Pt edges (from Te-1 to Te-8), e.g., the peaks of samples Te-1, Te-7, and Te-8 are located at 119.52, 117.49, and 115.93 cm^{-1}, respectively. This is due to the weakening of covalent atomic bonds within the Te chains with a unique chiral chain structure and the enhancement of interchain van der Waals interactions.[31,32] In addition, the red shifts of the A_1 peak in samples Te-7 and Te-8 are more pronounced, indicating that their interchain van der Waals forces are significantly enhanced,[27] which is consistent with their higher densities and severe adhesion of NWs as shown in Figure 3. Figure 4b shows the XRD patterns of A-Te NWs grown on Pt/PI/glass substrates with different pattern sizes, with evident amorphous diffuse scattering bulge peaks at 2θ = 15−30° for the PI/glass substrates. The A-Te NWs exhibit (100), (101), and (102) diffraction peaks at 2θ = 23.1°, 27.6°, and 38.3°, which are attributed to the trigonal phase of Te, respectively (JCPDS Card No. 36-1452).[33] In addition, the intensity of the Te diffraction peaks is enhanced (from Te-1 to Te-8) as the edge length of Pt patterns decreases gradually, indicating an increase of the Te content for a certain growth area. This result is consistent with the phenomena observed in the SEM images.

TEM characterizations were carried out to clarify the crystal structure of the Te NWs, and the results are shown in Figure 4c and 4d. Figure 4d exhibits the HRTEM image of an individual Te NW that is being presented in Figure 4c, and the perfectly aligned lattice fringes demonstrate the high crystallinity of the synthesized Te NWs. The measured interplanar spacing is approximately 0.31 nm, which matches the (101) plane of hexagonal Te (JCPDS no. 36-1452). This result confirms that the obtained Te NWs are single-crystalline and grow along the *c*-axis.

Optimizing the Synthesis Parameters

As shown in Figure 3c, A-Te NWs are only grown inside Pt patterns, owing to Pt's decisive role as a catalyst and a provider of nucleation sites for Te NW growth. To further study the effects of Pt layers on the growth of A-Te NWs, the influence of Pt thickness on the morphology of A-Te NWs is explored. Figure S3 shows the SEM images of A-Te NWs grown on Pt layers with different thicknesses. When the Pt thickness is 1 nm, only a few Te NWs and Te nanoparticles are located on the substrate, which indicates that Pt layers at this thickness cannot provide sufficient nucleation sites for the growth of A-Te NWs (Figure S3a). When the Pt thickness is increased to 2 nm, more inclined and sparser A-Te NWs are obtained (Figure S3b). Further increasing the Pt thickness to 3 nm, the density of A-Te NWs increases significantly (Figure S3c). However, there is no significant change in the growth density of A-Te NWs when the Pt thickness is further increased, which can be attributed to the fact that a 3 nm thick Pt layer has provided sufficient catalytically active sites within the region. Moreover, the array surface is covered with NWs detached from the substrate, which decreases the ordering of the NWs (Figure S3d,e). Therefore, a Pt thickness of 3 nm is the optimal thickness for the growth of A-Te NWs.

The liquid-phase reaction conditions for the growth of A-Te NWs were also explored, including the reaction time, the reaction temperature, the amount of the reducing agent, the pH values, and the effect of the CTAB concentration.

First, the effects of reaction time and reaction temperature were explored. Figure S4a−c shows the SEM images of A-Te NWs grown at different reaction times, indicating that the density of A-Te NWs increases with the extension of the reaction time. However, when the reaction time is extended to 8 h, some of the A-Te NWs grown at the Pt pattern edges start to fall off due to the long immersion time of the Pt/PI/glass

Downloaded from pubs.acs.org/langd5/article-pdf/42/39/29121/6858721/acs.langmuir.6c03602.pdf by TIANJIN UNIV user on 11 November 2026

https://doi.org/10.1021/acs.langmuir.6c03602
Langmuir 2026, 42, 29121−29130

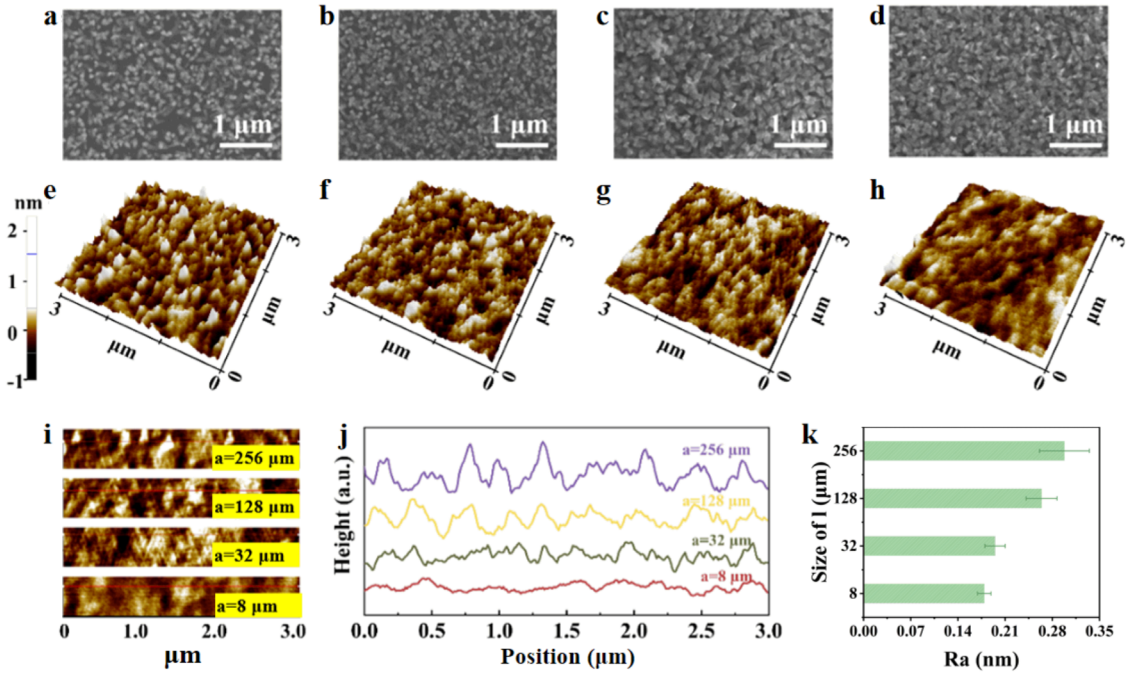


Figure 5. SEM images of A-Te NWs grown on square Pt patterns using optimized growth parameters, with side lengths of (a) 256 μm, (b) 128 μm, (c) 32 μm, and (d) 8 μm. (e–h) 3D AFM images of the corresponding Pt surfaces in (a–d); (i) line-sweep AFM images of the square Pt pattern surfaces in (e–h); (j) the line-sweep height profiles extracted from (i); (k) the roughness (Ra) of the square Pt pattern surfaces, extracted from (e–h).

substrate. Therefore, a reaction time of 6 h was found to be the best parameter for achieving highly dense A-Te NWs.

$$TeO_3^{2-} + N_2H_4 \rightarrow Te + N_2 + H_2O + 2OH^- \quad (1)$$

$$E = 0.59 + \frac{2.303RT}{4F}\{\log[TeO_3^{2-}][N_2H_4] - 2pH + 28\} \quad (2)$$

In addition, according to the redox reaction (eq 1) and the Nernst equation (eq 2), the reaction temperature, hydrazine hydrate concentration, and pH value all affect the rate of reaction. The SEM images for A-Te NWs grown at different reaction temperatures are shown in Figure S4d–f, where the A-Te NWs become tilted, and their vertical ordering decreases as the reaction temperature increases. This is because the reaction accelerates as the reaction temperature increases, resulting in decreased ordering of the A-Te NWs. Therefore, a low reaction temperature of 30 °C is more suitable for the vertical ordering of A-Te NWs.

Similarly, the amount of the reducing agent (hydrazine hydrate) also affects the kinetics of the redox reaction in solution and, thus, the morphology of A-Te NWs. According to eq 2, the reaction rate accelerates with the increase in concentration of hydrazine hydrate. Figure S5 shows the SEM images of A-Te NWs synthesized with different amounts of hydrazine hydrate. With an increase in the amount of hydrazine hydrate, the length of Te NWs gradually increases. When it reaches 3 mL, some of the Te NWs begin to tilt, weakening the vertical alignment of the A-Te NWs. Therefore, the addition of 2 mL of hydrazine hydrate in this reaction system is more favorable.

The reduction of sodium tellurite by hydrazine hydrate can be carried out under both alkaline and acidic conditions, but a faster reaction and an initial white flocculent suspension in the reaction solution under acidic conditions are unfavorable for the orderly growth of A-Te NWs.[34] Therefore, the effect of reaction solution pH under alkaline conditions is explored. Figure S6 shows SEM images of A-Te NWs grown at different pH values, where the tips of Te NWs become sharp, and the diameter increases when the pH of the reaction solution is increased from 8 to 10. Therefore, a pH of 10 is more suitable for promoting the uniformly ordered growth of A-Te NWs.

Given that surfactants are crucial for the morphology modulation of nanomaterials, the effect of CTAB concentration on the growth of A-Te NWs is explored. Figure S7 shows the SEM images of A-Te NWs grown at different CTAB concentrations. When no CTAB was added, the growth occurred in an uncontrolled manner, and two typical types of morphologies were observed: some NWs were connected with each other sideways to form sheet-like lamellar structures, and some NWs were clumped together to form thick NW bundles, as circled in Figure S6a. With the addition of 2.5 mM CTAB, the growth occurred in a controlled manner, and well-defined A-Te NWs were observed (Figure S7b). However, the concentration was not sufficient to fully control the growth process; as a result, some regions still showed a bundle-like morphology. When 5 mM CTAB was added, individual and nonaggregated A-Te NWs with uniform morphology were observed (Figure S7c). These phenomena indicate the structure-directing effect of CTAB on the growth of A-Te NWs, suppressing lateral growth and promoting the formation of one-dimensional structures.[35−37]

In the geometrically confined growth of Te NWs, adjusting the thickness of the platinum catalyst layer will change the interface energy between the catalyst substrate and the liquid-phase system, which thereby affects the nucleation density and alignment of A-Te NWs. The liquid-phase reaction conditions (reaction temperature, reaction time, reducing agent hydrazine hydrate concentration, and pH) can affect the kinetics of the

Downloaded from pubs.acs.org/langd5/article-pdf/42/39/29121/6858872/acs.langmuir.6c03602.pdf by TIANJIN UNIV user on 11 November 2026

https://doi.org/10.1021/acs.langmuir.6c03602
Langmuir 2026, 42, 29121−29130

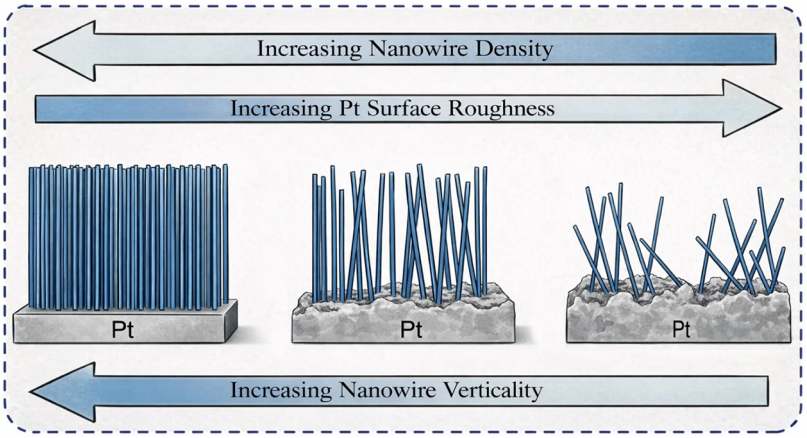


Figure 6. Schematic diagram demonstrating how the vertical ordering of Te NWs changes with the substrate roughness from a smooth to a coarse surface.

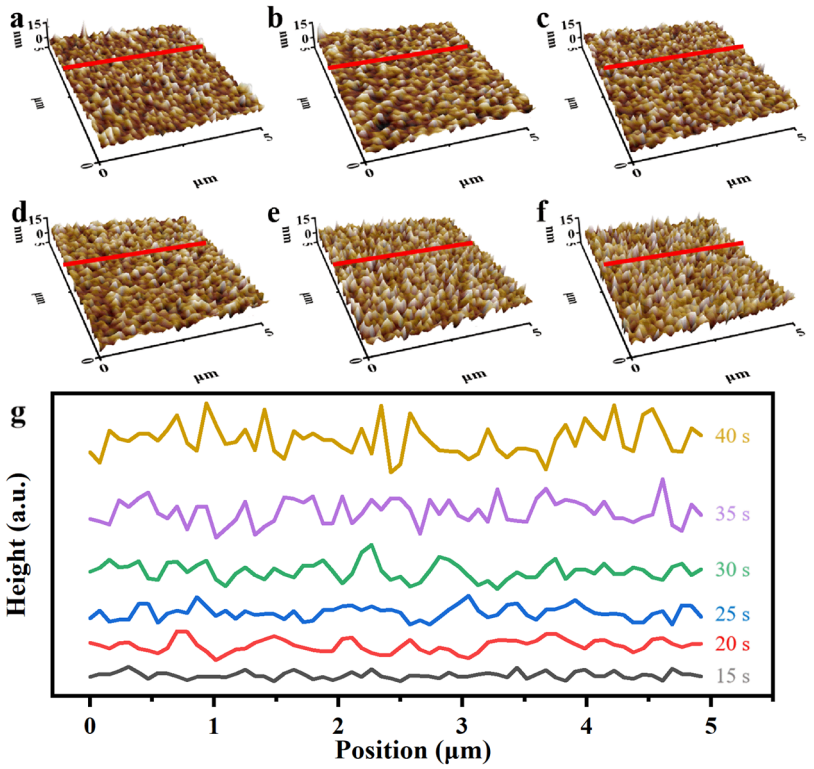


Figure 7. AFM topography of Pt catalyst layers after etching for (a) 15 s, (b) 20 s, (c) 25 s, (d) 30 s, (e) 35 s, and (f) 40 s; (g) comparison of surface fluctuations extracted along the red lines in (a–f).

chemical reactions involved in the growth of A-Te NWs. Therefore, optimizing these reaction parameters is helpful in finely regulating the growth rate, morphology, size distribution, and crystallinity of NWs.[38−40] By exploring the effects of the above parameters on the growth of A-Te NWs, a Pt layer thickness of 3 nm, a reaction time of 6 h, a reaction temperature of 30 °C, a pH of 10, a hydrazine hydrate amount of 2 mL, and a CTAB concentration of 5 mM were found to be the optimum conditions for the preparation of ordered A-Te NWs.

Effect of the Pt Catalyst Layer Morphology on the Growth of A-Te NWs

Beyond the thickness of the Pt catalyst layer and the liquid-phase reaction conditions, we also explored the effects of the Pt catalyst layer morphology on the growth of A-Te NWs. Figure 5a–d shows the SEM images of A-Te NWs grown on square Pt patterns with edge lengths of 256, 128, 32, and 8 μm under the optimized reaction conditions, where the density and verticality of the A-Te NWs exhibit distinct variations as the pattern size decreases. When the edge length of the square pattern is 256 μm, the NWs are vertically aligned, and the tips of the NWs are clearly visible (Figure 5a). However, the NWs are not densely packed or even absent in some regions. As the edge length is decreased to 128 μm, the NWs maintain high verticality with a significant improvement in the density of NWs (Figure 5b). With a further decrease in edge length to 32 μm, the NWs show enhanced density while maintaining high verticality (Figure 5c). For the smallest square Pt pattern with an edge length of 8 μm (Figure 5d), the tops of the A-Te NWs

https://doi.org/10.1021/acs.langmuir.6c03602
Langmuir 2026, 42, 29121−29130

Downloaded from pubs.acs.org/langd5/article-pdf/42/39/29121/6858872/1/acs.langmuir.6c03602.pdf by TIANJIN UNIV user on 11 November 2026

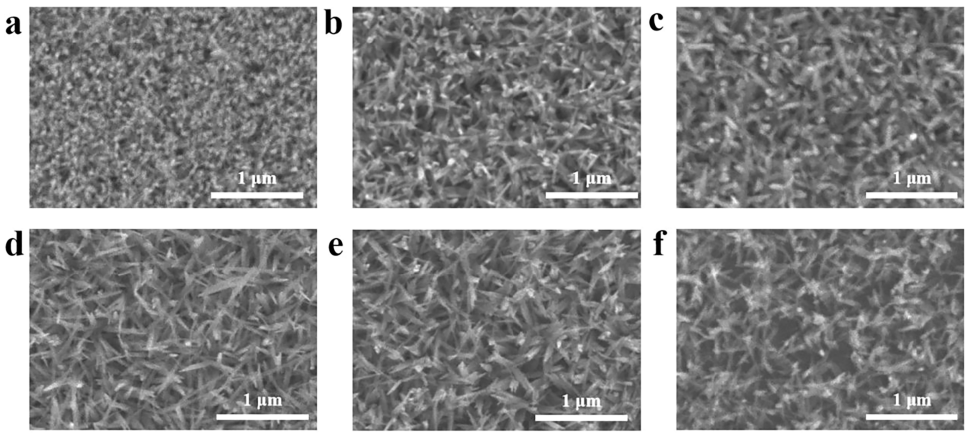


Figure 8. SEM images of A-Te NWs grown on Pt with roughness of (a) 0.44 nm, (b) 0.64 nm, (c) 1.26 nm, (d) 1.86 nm, (e) 2.57 nm, and (f) 2.92 nm.

were also discrete without any sticking, which suggests that the structure of A-Te NWs is more uniform. Moreover, optimization of the synthesis parameters greatly improved the vertical ordering and density of the NWs, and overcame the challenge of the sticking phenomena often observed in smaller patterns using unoptimized parameters. The SEM results indicate that the geometric confinement of the growth region is highly effective in obtaining highly dense and vertically ordered A-Te NWs.

As described above (Figure 4a), the geometric confinement leads to enhanced interchain van der Waals interactions among NWs, which facilitates the growth of vertically aligned NWS. To explore other factors influencing the growth of A-Te NWs, atomic force microscopy (AFM) was used to characterize Pt square arrays obtained from the same preparation process but with different edge lengths. Figure 5e–h shows the three-dimensional (3D) AFM images of square Pt patterns with edge lengths of 256, 128, 32, and 8 μm, where the surface roughness decreases with decreasing edge length. The 256 μm sample (Figure 5e) shows the roughest surface with large vertical excursions. Decreasing the edge length to 128 μm (Figure 5f) reduces both the number and the amplitude of surface protrusions. A further decrease to 32 μm (Figure 5g) produces a notably smoother morphology, while the 8 μm pattern (Figure 5h) exhibits the flattest surface. The corresponding AFM line-scan images and height profiles also demonstrate the same trend (Figure 5i,j), i.e., patterns with a greater edge length show larger surface fluctuation. The quantitative relationship between the roughness and the edge length is shown in Figure 5k. For edge lengths of 256, 128, 32, and 8 μm, the surface roughness was measured to be 0.298, 0.264, 0.195, and 0.179 nm, respectively.

The trend described above can be attributed to the geometrically constrained deposition of Pt during the patterning process, analogous to the geometrically constrained growth of two-dimensional transition-metal sulfide films.[41] A much more uniform thickness can be obtained when deposited in a small confined area than when deposited in a large area, since geometric confinement leads to a decrease in the surface roughness of the deposited films.[42] Interestingly, on a smooth Pt surface, the Te NWs grow vertically with high order. As the surface roughness increases, Te NWs begin to get entangled, although they still grow in an upward direction (Figure 6). Therefore, we infer that the roughness of Pt plays a key role in directing the growth of Te NWs.

To verify the above inference, we prepared Pt catalyst layers with the same area (50 μm × 50 μm), i.e., the same degree of geometric confinement, and precisely tuned their roughness via reactive ion etching (RIE). The etching gas, a mixture of O_2 and Ar (O_2:Ar = 3:1), can significantly alter the roughness of the organic PI substrate through the combined effect of chemical etching by O_2 and physical bombardment by Ar (Figure S8).[36,43,44] Then the etching effect was transferred to the above Pt film in the subsequent e-beam deposition step.

Figure 7a–f shows the AFM surface topography of Pt catalyst layers after different etching times. The sample etched for 15 s (Figure 7a) exhibits a relatively flat surface with only slight nanoscale fluctuations, showing the lowest roughness (0.44 nm). When the etching time is extended to 20 s (Figure 7b), the surface begins to develop subtle peak-and-valley structures, with the roughness slightly increasing to 0.64 nm. After 25 s of etching (Figure 7c), the surface undulations become significantly more pronounced, forming a distinct island-like or hillock-like morphology, with the roughness rising to 1.26 nm. Upon further extension to 30 s (Figure 7d), the surface features become coarser, with both the depth and lateral dimensions of the peaks and valleys increasing, and the roughness reaches 1.86 nm. The sample etched for 35 s (Figure 7e) displays much more vigorous surface undulations, featuring sharp ridge-like protrusions and deep trenches, with the roughness increasing to 2.57 nm. When the etching time reaches 40 s (Figure 7f), the surface morphology becomes the roughest, forming distinct three-dimensional raised-and-de-pressed structures, and the roughness attains its maximum value of 2.92 nm. Figure 7g shows the surface roughness fluctuations along the red lines in Figure 7a–f, where higher fluctuation corresponds to longer etching time.

Subsequently, A-Te NWs were grown on these Pt catalyst layers under the optimal growth conditions described earlier, with their SEM images shown in Figure 8. The SEM results show similar phenomena to those observed in Figure 5 and confirm that a smoother Pt surface promotes the growth of Te NWs with higher ordering and density. When the surface roughness is lower, the tips of the nanowires are clearly visible, and the nanowires are densely packed (Figure 8a). As the substrate roughness increases from 0.44 to 0.64 nm, the nanowires begin to tilt, and vertical ordering decreases (Figure

https://doi.org/10.1021/acs.langmuir.6c03602
Langmuir 2026, 42, 29121−29130

Downloaded from pubs.acs.org/langd5/article-pdf/42/39/29121/6858872/1/acs.langmuir.6c03602.pdf by TIANJIN UNIV user on 11 November 2026

8b). As the surface roughness increases to 1.26 nm (Figure 8c), the nanowires begin to deviate from their initial vertical orientation, with the tips of adjacent nanowires crossing each other while the overall array density remains at a moderate level. When the roughness further increases to 1.86 nm (Figure 8d), the nanowires become noticeably intertwined, and the array density decreases significantly, accompanied by the emergence of small bare areas on the substrate. As the roughness reaches 2.57 nm (Figure 8e), the nanowire array becomes highly disordered, with most nanowires collapsed. When the surface roughness reaches 2.92 nm, the density of the nanowires decreases significantly, with a larger number of void regions where there are no nanowires. These results clearly indicate that, under identical geometric confinement, the increase in the surface roughness of the catalyst layer significantly reduces the vertical ordering and density of the nanowires (Figure 8f).

Quantitative analysis of the SEM morphology images was performed by using a self-developed image processing program. The image recognition program, implemented based on the OpenCV library, utilizes a combination of Canny edge detection and Hough transform methods to analyze the density of NWs. It was observed that as the substrate surface roughness increased, the density of the NWs exhibited a systematic decreasing trend (Figure S9). A pixel-based recognition statistical method was used to quantitatively evaluate the nanowire distribution in samples with different roughness levels, with the results shown in Table 1.

Table 1. Relationship between Different Roughness and the Density of Grown Nanowires

Surface roughness (Ra, nm)	0.44	0.64	1.26	1.86	2.57	2.92
Nanowire density (%)	43.3	40.7	38.8	37.9	36.9	34.4

To quantitatively assess the sample tilt, we analyzed SEM images acquired at varying tilt angles. The projected morphology of surface features (e.g., boundaries and protrusions) changes systematically with tilt: larger angles produce longer, higher-fraction boundary segments that appear as straight lines in the projection. We, therefore, adopted the straight-edge length extracted from images as a quantitative metric for tilt degree. Prior to analysis, all original RGBA images were converted to grayscale and subjected to Gaussian filtering (σ = 1) for noise reduction. The processed images (Figure S10a–f) were then analyzed for straight-edge length and global Hough-transform-based straightness (Figure S10g). The results show that the edge straightness S increases gradually with catalyst surface roughness. To provide an independent, whole-image validation, we applied a Probabilistic Hough Transform to the extracted edge contours to calculate the fraction of edge pixels covered by detected straight-line segments, which corroborates the findings from the straight-edge statistical analysis.

The above morphological evolution trend indicates that substrate surface roughness has a critical impact on the vertical orientation and density of the NWs. By controlling the PI surface roughness, the roughness of the Pt layer can be altered, as well as the growth behavior and final morphological characteristics of the NWs.

CONCLUSIONS

In conclusion, ordered Te nanowire arrays were successfully grown on Pt/PI/glass substrates by using a seedless chemical liquid-phase method, and the optimal conditions for achieving vertically ordered Te nanowire arrays were determined. Square Pt catalytic layers were found to play an important role in the geometrically confined growth of A-Te NWs: their roughness dictates the vertical ordering of Te NWs, providing a flexible approach to optimizing the structural features of NWs. This study provides an efficient approach for growing highly ordered Te nanowire arrays and facilitates their practical applications.

EXPERIMENTAL PROCEDURES

Chemicals

All chemicals were used as received without further purification unless otherwise specified. Tellurium dioxide (TeO_2, 99.99%), hydrazine monohydrate ($N_2H_4{\cdot}H_2O$, 80%), cetyltrimethylammonium bromide (CTAB, 99%), ethylenediaminetetraacetic acid disodium salt (EDTA-Na_2, 98%), sodium hydroxide (NaOH, 96%), and *N*,*N*-dimethylformamide (DMF, 99.8%) were purchased from Shanghai Aladdin Bio-Chem Technology Co., LTD. Ammonium hydroxide ($NH_3{\cdot}H_2O$, 25%) was ordered from Tianjin Yuanli Chemical Co., LTD. Concentrated nitric acid (HNO_3, 68%) was bought from Tianjin Beilian Fine Chemicals Development Co., Ltd. Polyimide (PI) was bought from Beijing Huawei Ruike Chemical Co., LTD. Glass (CAT.NO.7105) was bought from Yancheng Feizhou Glass Co., LTD.

Preparation of Pt/PI/Glass Substrates and A-Te NWs/Pt/PI/Glass

1 cm × 1 cm plain glass slides were sequentially ultrasonically cleaned with acetone, ethanol, and deionized water to remove surface impurities. The DMF-diluted polyimide liquid (PI:DMF = 2:1) was spin-coated on the glass slide at 2000 rpm, and then annealed in vacuum in a tube heating furnace, with parameters of 60 °C−30 min, 166 °C−10 min, and 300 °C−15 min, to obtain a PI/glass substrate. Then, square Pt arrays with a certain total area but different side length sizes were prepared on the substrate by photolithography and electron beam vaporization. The thickness of the electron-beam-vaporized Pt layer was controlled by adjusting the deposition time with a deposition rate of 0.02 Å s^{-1}.

Synthesis of A-Te NWs on Pt/PI/Glass Substrate

The specific steps were as follows: 25 mL of distilled water, 2 mL of $NH_3{\cdot}H_2O$, and 0.145 g of EDTA-Na_2 were added to a glass beaker to form solution A. 20 mL of distilled water, 50 mg of NaOH, and 80 mg of TeO_2 were added to another glass beaker to form a clear solution B. 5 mM CTAB was added to solution B. Solution B was slowly added to the stirring solution A to form a mixture and concentrated nitric acid was used to adjust the pH to 10. 2 mL of hydrazine hydrate ($N_2H_4{\cdot}H_2O$, 80 wt %) was added to the above mixture, and after stirring for 2 min, the Pt/PI/glass substrate was immersed in the solution with the Pt side facing down. The glass beaker was sealed with the polyethylene wrap and transferred to an oven at 30 °C for the reaction. After 6 h of reaction, the A-Te NWs/Pt/PI/glass substrate was taken out and cleaned with distilled water. After cleaning, the samples were placed in a vacuum oven and dried at 50 °C for 2 h.

Characterization and Measurements

The surface morphology and element composition of the samples were characterized by scanning electron microscopy (SEM, SU3500, Hitachi, Japan) and an energy-dispersive spectrometer (EDS, model 550i, IXRF, America). The surface roughness of the Pt/PI/glass substrates was measured before A-Te NW growth by atomic force microscopy (AFM, NX10, Park, South Korea) in non-contact mode. An X-ray powder diffractometer (XRD, TD-3500 model) was used for

Downloaded from pubs.acs.org/langd5/article-pdf/42/39/29121/6858872/1/acs.langmuir.6c03602.pdf by TIANJIN UNIV user on 11 November 2026

https://doi.org/10.1021/acs.langmuir.6c03602
Langmuir 2026, 42, 29121−29130

crystallinity analysis. The pH values were measured by a pH meter (S210, Mettler Toledo Instruments (Shanghai) Co., LTD). The Raman spectra were recorded by the Raman spectrometer (RTS-2) at a 638 nm laser wavelength.

■ ASSOCIATED CONTENT

Supporting Information

The Supporting Information is available free of charge at https://pubs.acs.org/doi/10.1021/acs.langmuir.6c03602.

SEM images and roughness data; physical photographs of samples Te-1, Te-2, Te-3, Te-4, Te-5, Te-6, Te-7, and Te-8 (PDF)

■ AUTHOR INFORMATION

Corresponding Authors

Yanqing Ma − *Tianjin International Center for Nanoparticles and Nanosystems, Tianjin University, Tianjin 300072, P. R. China; Tianjin Key Laboratory of Low-Dimensional Electronic Materials and Advanced Instrumentation, Tianjin 300072, P. R. China; Haihe Laboratory for Low-Dimensional Electronic Materials, Tianjin 300074, P. R. China; School of Precision Instrument and Optoelectronics Engineering, Tianjin University, Tianjin 300072, P. R. China;* orcid.org/0000-0002-3317-8273; Email: mayanqing@tju.edu.cn

Lei Ma − *Tianjin International Center for Nanoparticles and Nanosystems, Tianjin University, Tianjin 300072, P. R. China; Tianjin Key Laboratory of Low-Dimensional Electronic Materials and Advanced Instrumentation, Tianjin 300072, P. R. China; Haihe Laboratory for Low-Dimensional Electronic Materials, Tianjin 300074, P. R. China;* orcid.org/0000-0002-2446-4833; Email: lei.ma@tju.edu.cn

Authors

Xiaobing Zhu − *Tianjin International Center for Nanoparticles and Nanosystems, Tianjin University, Tianjin 300072, P. R. China*

Moneeb Zafar − *Tianjin International Center for Nanoparticles and Nanosystems, Tianjin University, Tianjin 300072, P. R. China*

Yanmei Ren − *Tianjin International Center for Nanoparticles and Nanosystems, Tianjin University, Tianjin 300072, P. R. China*

Rongke Sun − *Tianjin International Center for Nanoparticles and Nanosystems, Tianjin University, Tianjin 300072, P. R. China*

Rui Li − *Tianjin International Center for Nanoparticles and Nanosystems, Tianjin University, Tianjin 300072, P. R. China*

Xin He − *Tianjin International Center for Nanoparticles and Nanosystems, Tianjin University, Tianjin 300072, P. R. China;* orcid.org/0000-0001-7009-2826

Complete contact information is available at: https://pubs.acs.org/10.1021/acs.langmuir.6c03602

Author Contributions

⊥X.Z. and M.Z. contributed equally to this work.

Notes

The authors declare no competing financial interest.

■ ACKNOWLEDGMENTS

This work was financially supported by the National Key R&D Program of China (No. 2022YFC3006303), the Tianjin National Science Foundation Project (No. 25JCZDJC01380), and the Innovation Fund of the Haihe Laboratory of Low-dimensional Electronic Materials (25HHDWSS00005).

■ REFERENCES

(1) Yang, L.; Gordon, M. P.; Menon, A. K.; Bruefach, A.; Haas, K.; Scott, M. C.; Prasher, R. S.; Urban, J. J. Decoupling Electron and Phonon Transport in Single-Nanowire Hybrid Materials for High-Performance Thermoelectrics. *Sci. Adv.* **2021**, *7* (20), No. eabe6000.

(2) Meng, Q.; Song, H.; Du, Y.; Ding, Y.; Cai, K. Facile Preparation of Poly(3,4-Ethylenedioxythiophene): Poly(Styrenesulfonate)/Ag2Te Nanorod Composite Films for Flexible Thermoelectric Generator. *J. Materiomics* **2021**, *7* (2), 302−309.

(3) Zha, J.; Dong, D.; Huang, H.; Xia, Y.; Tong, J.; Liu, H.; Chan, H. P.; Ho, J. C.; Zhao, C.; Chai, Y.; Tan, C. Electronics and Optoelectronics Based on Tellurium. *Adv. Mater.* **2024**, *36* (45), No. 2408969.

(4) Park, M.; Lyu, Z.; Song, S. H.; Lee, H.-J. Controlled Synthesis of Tellurium Nanowires and Performance Optimization of Thin-Film Transistors via Percolation Network Engineering. *Nanomaterials* **2025**, *15* (14), No. 1128.

(5) Liu, Y.; Jiang, Q.; Zhang, J.; Ding, W.; Xu, J.; Liu, P.; Nie, G.; Mao, H.; Jiang, F. Green Synthesis of Air-Stable Tellurium Nanowires via Biomolecule-Assisted Hydrothermal for Thermoelectrics. *Mater. Adv.* **2020**, *1* (5), 1125−1133.

(6) Wang, Z.; Tan, C.; Peng, M.; Yu, Y.; Zhong, F.; Wang, P.; He, T.; Wang, Y.; Zhang, Z.; Xie, R.; Wang, F.; He, S.; Zhou, P.; Hu, W. Giant Infrared Bulk Photovoltaic Effect in Tellurene for Broad-Spectrum Neuromodulation. *Light Sci. Appl.* **2024**, *13* (1), No. 277.

(7) Kim, S.; Kim, I. H.; Fattahimoghaddam, H.; Cho, M.-K.; Jeong, Y. J.; Lee, W. Copper-Doped Tellurium Nanowire-Based Gas Sensor for Chemiresistive Detection of Nitrogen Dioxide. *Sens. Actuators, B* **2025**, *433* (101), No. 137587.

(8) Wang, S.; Higashitarumizu, N.; Jamal, M.; Babbe, F.; Chrzan, D. C.; Scott, M. C.; Javey, A. Mid-Infrared Photoluminescence from Tellurium Thin Films. *Nano Lett.* **2025**, *25* (23), 9311−9317.

(9) Zeng, X.; Ren, L.; Xie, J.; Mao, D.; Wang, M.; Zeng, X.; Du, G.; Sun, R.; Xu, J.-B.; Wong, C.-P. Room-Temperature Welding of Silver Telluride Nanowires for High-Performance Thermoelectric Film. *ACS Appl. Mater. Interfaces* **2019**, *11* (41), 37892−37900.

(10) Liu, H.; Zeng, B.; Jia, F. Direct Growth of Tellurium Nanorod Arrays on Pt/FTO/Glass through a Surfactant-Assisted Chemical Reduction. *Nanotechnology* **2011**, *22* (30), No. 305608.

(11) Xu, J.; Refino, A. D.; Delvallée, A.; Seibert, S.; Schwalb, C.; Hansen, P. E.; Foldyna, M.; Siaudinyte, L.; Hamdana, G.; Wasisto, H. S.; Kottmeier, J.; Dietzel, A.; Weimann, T.; Prüssing, J. K.; Bracht, H.; Peiner, E. Deep-Reactive Ion Etching of Silicon Nanowire Arrays at Cryogenic Temperatures. *Appl. Phys. Rev.* **2024**, *11* (2), No. 021411.

(12) McCormack, K.; Schaper, N.; Kim, Y.; Hensley, D. K.; Kravchenko, I.; Lavrik, N. V.; Gosztola, D. J.; Pantano, M. F.; Kuljanishvili, I. Enabling a Novel Approach to a Controlled Fabrication of 1D Crystalline Nanowires on Suspended Microstructures of Arbitrary Geometries Using Two Direct-Writing Technologies. *Mater. Today Nano* **2022**, *20* (102), No. 100241.

(13) Haifeng, X.; Chengyi, H.; Qinghong, Z.; Yaogang, L.; Hongzhi, W. Preparation and Thermoelectric Performance of Tellurium Nanowires-Based Thin-Film Materials. *J. Inorg. Mater.* **2020**, *35* (9), 1034−1040.

(14) Li, Z. P.; Xu, Z. M.; Qu, X. P.; Wang, S. B.; Peng, J.; Mei, L. H. Fabrication of Nanopore and Nanoparticle Arrays with High Aspect Ratio AAO Masks. *Nanotechnology* **2017**, *28* (9), No. 095301.

(15) Karalis, G.; Tzounis, L.; Mytafides, C. K.; Tsirka, K.; Formanek, P.; Stylianakis, M.; Kymakis, E.; Paipetis, A. S. A High Performance Flexible and Robust Printed Thermoelectric Generator Based on

Downloaded from pubs.acs.org/langd5/article-pdf/42/39/29121/6858721/acs.langmuir.6c03602.pdf by TIANJIN UNIV user on 11 November 2026

Hybridized Te Nanowires with PEDOT:PSS. *Appl. Energy* **2021**, *294*, No. 117004.
(16) Zhao, C.; Batiz, H.; Yasar, B.; Ji, W.; Scott, M. C.; Chrzan, D. C.; Javey, A. Orientated Growth of Ultrathin Tellurium by van Der Waals Epitaxy. *Adv. Mater. Interfaces* **2022**, *9* (5), No. 2101540.
(17) Sun, L.; Yuan, G.; Gao, L.; Yang, J.; et al. Chemical Vapour Deposition. *Nat. Rev. Methods Primers* **2021**, *1* (1), No. 5.
(18) Park, D.; Ju, H.; Kim, J. Enhanced Thermoelectric Properties of Flexible N-Type Ag2Se Nanowire/Polyvinylidene Fluoride Composite Films Synthesized via Solution Mixing. *J. Ind. Eng. Chem.* **2021**, *93*, 333−338.
(19) Li, H.; Liu, Y.; Li, P.; Liu, S.; Du, F.; He, C. Enhanced Thermoelectric Performance of Carbon Nanotubes/Polyaniline Composites by Multiple Interface Engineering. *ACS Appl. Mater. Interfaces* **2021**, *13* (5), 6650−6658.
(20) Ren, Y.; Sun, R.; Yu, X.; Wang, R.; Zhang, W.; Zhu, X.; Ma, Y.; Ma, L. A Systematic Study on Synthesis Parameters and Thermoelectric Properties of Tellurium Nanowire Bundles. *Mater. Adv.* **2023**, *4* (19), 4455−4462.
(21) Wang, R.; He, Z.; Wang, J.-L.; Liu, J.-Y.; Liu, J.-W.; Yu, S.-H. Manipulating Nanowire Structures for an Enhanced Broad-Band Flexible Photothermoelectric Photodetector. *Nano Lett.* **2022**, *22* (14), 5929−5935.
(22) Yu, X.; Hu, C.; Ji, P.; Ren, Y.; Zhao, H.; Liu, G.; Xu, R.; Zhu, X.; Li, Z.; Ma, Y.; Ma, L. Optically Transparent Ultrathin NiCo Alloy Oxide Film: Precise Oxygen Vacancy Modulation and Control for Enhanced Electrocatalysis of Water Oxidation. *Appl. Catal., B* **2022**, *310*, No. 121301.
(23) Peng, C.; Zhou, T.; Wei, P.; Xu, W.; Pan, H.; Peng, F.; Jia, J.; Zhang, K.; Yu, H. Photocatalysis over MXene-Based Hybrids: Synthesis, Surface Chemistry, and Interfacial Charge Kinetics. *APL Mater.* **2021**, *9* (7), No. 070703.
(24) Xu, S.; Lao, C.; Weintraub, B.; Wang, Z. L. Density-Controlled Growth of Aligned ZnO Nanowire Arrays by Seedless Chemical Approach on Smooth Surfaces. *J. Mater. Res.* **2008**, *23* (8), 2072−2077.
(25) Koverga, A. A.; Flórez, E.; Gómez−Marín, A. M. Electronic Changes at the Platinum Interface Induced by Bismuth and Tellurium Adatom Adsorption. *Appl. Surf. Sci.* **2023**, *608*, No. 155137.
(26) Chu, C.; Wang, Y.; Ma, Y. Unraveling the Growth Mechanism of Chiral Inorganic Nanocrystals via High-Resolution Electron Microscopy. *J. Am. Chem. Soc.* **2024**, *146* (51), 35339−35346.
(27) Son, G.; Kim, S.; Kim, J. Exchange-Correlation Functional Effects on Electronic and Phononic Band Structures of Helical Se and Te. *Curr. Appl. Phys.* **2026**, *82*, 22−29.
(28) Weiss, N. O.; Duan, X. A Guide for Nanowire Growth. *Proc. Natl. Acad. Sci. U.S.A.* **2013**, *110* (38), 15171−15172.
(29) Kang, M.; Jeong, H. B.; Shim, Y.; Chai, H.-J.; Kim, Y.-S.; Choi, M.; Ham, A.; Park, C.; Jo, M.; Kim, T. S.; Park, H.; Lee, J.; Noh, G.; Kwak, J. Y.; Eom, T.; Lee, C.-W.; Choi, S.-Y.; Yuk, J. M.; Song, S.; Jeong, H. Y.; Kang, K. Layer-Controlled Growth of Single-Crystalline 2D Bi_2O_2Se Film Driven by Interfacial Reconstruction. *ACS Nano* **2024**, *18* (1), 819−828.
(30) Duan, Y.; Zhao, D.; Li, Z.; Yu, J.; Liang, Y.; Wang, Y. Angle-Resolved Raman Scattering Study of Anisotropic Two-Dimensional Tellurium Nanoflakes. *J. Appl. Phys.* **2025**, *137* (2), No. 024301.
(31) Qin, J.-K.; Liao, P.-Y.; Si, M.; Gao, S.; Qiu, G.; Jian, J.; Wang, Q.; Zhang, S.-Q.; Huang, S.; Charnas, A.; Wang, Y.; Kim, M. J.; Wu, W.; Xu, X.; Wang, H.-Y.; Yang, L.; Khin Yap, Y.; Ye, P. D. Raman Response and Transport Properties of Tellurium Atomic Chains Encapsulated in Nanotubes. *Nat. Electron.* **2020**, *3* (3), 141−147.
(32) Li, J.; Yang, Q.; He, D.; Wang, Y.; Hwang, E.; Yang, Y. Morphology-Controlled Synthesis, Growth Mechanism, and Applications of Tellurium Nanostructures. *Mater. Adv.* **2024**, *5* (19), 7548−7560.
(33) Zuo, Y.; Li, T.; Rao, D.; Lei, X.; Li, Q.; Zhu, G.; Lu, R.; Han, H. Synthesis of Tellurium Fusiform Nanoarchitectures by Controlled Living Nanowire Modification. *J. Phys. Chem. C* **2016**, *120* (22), 12305−12312.
(34) Amiri, P.; Behin, J. Fate of Nanoparticles in Aqueous Environments: Stability, Physicochemical Interactions, and Separation. *Sci. Total Environ.* **2025**, *1007*, No. 180882.
(35) Ashraf, W.; Fatima, T.; Srivastava, K.; Khanuja, M. Superior Photocatalytic Activity of Tungsten Disulfide Nanostructures: Role of Morphology and Defects. *Appl. Nanosci.* **2019**, *9* (7), 1515−1529.
(36) Liu, G.; Xu, Y.; Xu, C.; Basile, A.; Wang, F.; Dhar, S.; Conrad, E.; Mooney, P.; Gustafsson, T.; Feldman, L. C. Effects and Mechanisms of RIE on SiC Inversion Layer Mobility and Its Recovery. *Appl. Surf. Sci.* **2015**, *324*, 30−34.
(37) Xie, W.; Zhu, K.; Jiang, W.; Yang, H.; Ma, M.; Zhao, L.; Yang, W. Highly 002-Oriented Dendrite-Free Anode Achieved by Enhanced Interfacial Electrostatic Adsorption for Aqueous Zinc-Ion Batteries. *ACS Nano* **2024**, *18* (32), 21184−21197.
(38) Pallotta, R.; Degani, M.; Toniolo, F.; Cavalli, S.; Turci, F.; Bi, W. H.; Girella, A.; Milanese, C.; Schüler, A.; Magrez, A.; Grancini, G. On the Synergistic Interplay between Annealing Temperature and Time and Additive Concentration for Efficient and Stable FAPbI3 Perovskite Solar Cells. *Mater. Today Adv.* **2024**, *24*, No. 100541.
(39) Halfwerk, R.; Yntema, D.; Van Spronsen, J.; Keesman, K.; Van der Padt, A. Crystallization Kinetics of Lactose Recovered at Sub-Zero Temperatures: A Population Balance Model Combining Mutarotation, Nucleation and Crystal Growth. *J. Food Eng.* **2023**, *345*, No. 111412.
(40) Cai, X.; Xu, Y.; Liu, M.; Cao, B.; Li, X. Study of the Growth Kinetics of in Situ WC Grains in Tungsten Carbide Layers Produced by a Diffusion-Controlled Reaction. *Ceram. Int.* **2022**, *48* (23), 35290−35300.
(41) Kim, K. S.; Seo, S.; Kwon, J.; Lee, D.; Kim, C.; Ryu, J.-E.; Kim, J.; Suh, J. M.; Jung, H.-G.; Jo, Y.; Shin, J.-C.; Song, M.-K.; Feng, J.; Ahn, H.; Lee, S.; Cho, K.; Jeon, J.; Seol, M.; Park, J.-H.; Kim, S. W.; Kim, J. Growth-Based Monolithic 3D Integration of Single-Crystal 2D Semiconductors. *Nature* **2024**, *636* (8043), 615−621.
(42) Kim, K. S.; Lee, D.; Chang, C. S.; Seo, S.; Hu, Y.; Cha, S.; Kim, H.; Shin, J.; Lee, J.-H.; Lee, S.; Kim, J. S.; Kim, K. H.; Suh, J. M.; Meng, Y.; Park, B.-I.; Lee, J.-H.; Park, H.-S.; Kum, H. S.; Jo, M.-H.; Yeom, G. Y.; Cho, K.; Park, J.-H.; Bae, S.-H.; Kim, J. Non-Epitaxial Single-Crystal 2D Material Growth by Geometric Confinement. *Nature* **2023**, *614* (7946), 88−94.
(43) Tintelott, M.; Schander, A.; Lang, W. Understanding Electrical Failure of Polyimide-Based Flexible Neural Implants: The Role of Thin Film Adhesion. *Polymers* **2022**, *14* (18), No. 3702.
(44) Ahmed, S. F.; Lee, K.-R.; Yoon, J.; Moon, M.-W. Nanoporous Structures of Polyimide Induced by Ar Ion Beam Irradiation. *Appl. Surf. Sci.* **2012**, *258* (8), 3841−3845.

Downloaded from pubs.acs.org/langd5/article-pdf/42/39/29121/6858872/1/acs.langmuir.6c03602.pdf by TIANJIN UNIV user on 11 November 2026

https://doi.org/10.1021/acs.langmuir.6c03602
Langmuir 2026, 42, 29121−29130